Chemical Science

ROYAL SOCIETY OF CHEMISTRY

EDGE ARTICLE

View Article Online
View Journal | View Issue

Cite this: *Chem. Sci.*, 2022, **13**, 9256

All publication charges for this article have been paid for by the Royal Society of Chemistry

Heterostructured FeNi hydroxide for effective electrocatalytic oxygen evolution†

Fayan Li,[ab] Yanyan Li,[ab] Lei Li,[ab] Wen Luo,[c] Zhouguang Lu,[c] Xinyu Zhang*[ab] and Zhiping Zheng *[ab]

Hydrogen production technology by water splitting has been heralded as an effective means to alleviate the envisioned energy crisis. However, the overall efficiency of water splitting is limited by the effectiveness of the anodic oxygen evolution reaction (OER) due to the high energy barrier of the $4e^-$ process. The key to addressing this challenge is the development of high-performing catalysts. Transition-metal hydroxides with high intrinsic activity and stability have been widely studied for this purpose. Herein, we report a gelatin-induced structure-directing strategy for the preparation of a butterfly-like FeNi/Ni heterostructure (FeNi/Ni HS) with excellent catalytic performance. The electronic interactions between Ni^{2+} and Fe^{3+} are evident both in the mixed-metal "torso" region and at the "torso/wing" interface with increasing Ni^{3+} as a result of electron transfer from Ni^{2+} to Fe^{3+} mediated by the oxo bridge. The amount of Ni^{3+} also increases in the "wings", which is believed to be a consequence of charge balancing between Ni and O ions due to the presence of Ni vacancies upon formation of the heterostructure. The high-valence Ni^{3+} with enhanced Lewis acidity helps strengthen the binding with OH^- to afford oxygen-containing intermediates, thus accelerating the OER process. Direct evidence of FeNi/Ni HS facilitating the formation of the Ni–OOH intermediate was provided by *in situ* Raman studies; the intermediate was produced at lower oxidation potentials than when $Ni_2(CO_3)(OH)_2$ was used as the reference. The Co congener (FeCo/Co HS), prepared in a similar fashion, also showed excellent catalytic performance.

Received 17th May 2022
Accepted 13th July 2022

DOI: 10.1039/d2sc02767d

rsc.li/chemical-science

Introduction

With the increasing challenges associated with the energy crisis and environmental pollution, it is of paramount significance to develop renewable and clean energies.[1–3] Hydrogen gas, with its high energy density and sole combustion product being water, is considered as the most attractive energy carrier.[4,5] Water splitting has been the primary means for hydrogen production. The process entails two half-reactions, namely the hydrogen evolution reaction (HER) and the oxygen evolution reaction (OER). The OER, involving four electrons in the process, occurs at the anode and is recognized as the "bottleneck" challenge due to its sluggish kinetics.[6–8] Transition-metal hydroxides with high intrinsic activity and stability in the presence of alkaline electrolytes have been the focus of recent research as potential efficient electrocatalysts to address this challenge.[9–13] When compared with single-metal hydroxides, bimetallic hydroxides are more attractive due to the possible electronic interactions between the two different metal sites that may lead to the fine-tuning of the electronic properties of the active sites for improvement of catalytic properties and the resulting facilitated generation and transformation of oxy-containing intermediates.[14–17] Impressive progress notwithstanding, the presently known bimetallic hydroxides have yet to meet the standard for desirable performance; further development in this vein is thus warranted.

Constructing heterointerfaces and relying on the anticipated synergy between the components is a general strategy for obtaining high-performing catalysts.[18–21] Traditional strategies for constructing heterostructures include the soft-template method,[22] hydrothermal synthesis,[23,24] electrodeposition,[25–27] and electrostatic adsorption.[28] However, most of these methods involve multiple steps that are generally complicated and energy-consuming, and are not suitable for large-scale preparation. Therefore, a simple, low-cost, and universally applicable strategy is highly desirable for the preparation of bimetallic heterostructured hydroxides. Gelatin, a biodegradable and environmentally friendly surfactant, is rich in functional groups (–CO–NH_2, –COOH, –NH_2) that are capable of coordinating various metal ions to induce directional growth of molecular and material structures with different chemical compositions and morphologies.[29–32]

With this recognition, a butterfly-like bimetallic FeNi/Ni hydroxide heterostructure (FeNi/Ni HS) featuring a mixed-

[a]*Department of Chemistry, Guangdong Provincial Key Laboratory of Energy Materials for Electric Power, Southern University of Science and Technology (SUSTech), Shenzhen 518055, China. E-mail: zhangx1@sustech.edu.cn; zhengzp@sustech.edu.cn*

[b]*Key Laboratory of Energy Conversion and Storage Technologies, SUSTech, Ministry of Education, Shenzhen 518055, China*

[c]*Department of Materials Science and Engineering, SUSTech, Shenzhen 518055, China*

† Electronic supplementary information (ESI) available. See https://doi.org/10.1039/d2sc02767d

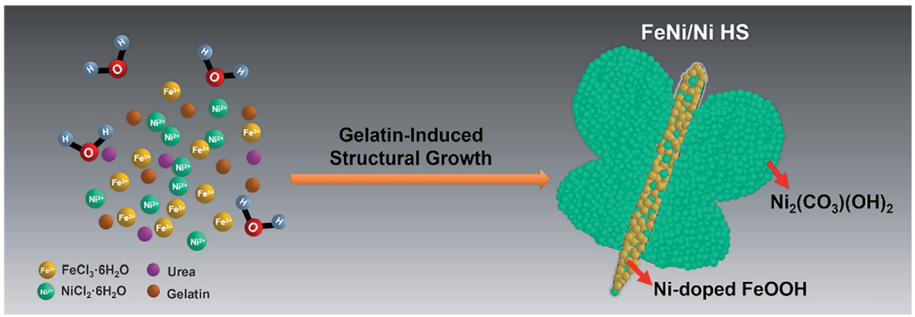

Scheme 1 Schematic illustration showing the gelatin-induced synthetic process for FeNi/Ni HS.

metal (FeNi) "torso" and two "wings" of pure Ni with "torso–wing" (FeNi) interfaces was successfully prepared by gelatin-induced preparation (Scheme 1). We showed its excellent electrocatalytic performance for the OER by a series of comparative studies with reference to its single-metal (Ni and Fe) analogs. Its electronic structure was analyzed by using X-ray photoelectron spectroscopy (XPS) and electron energy loss spectroscopy (EELS) from which the Ni^{2+}-to-Fe^{3+} electron transfer *via* the oxo bridge can be inferred. The resulting increase of Ni^{3+}, together with the Ni vacancies facilitates the formation of Ni–OOH – the key intermediate preceding the release of O_2 as revealed by *in situ* Raman spectroscopy.

Results and discussion

Structural and morphological characterization

The XRD pattern of FeNi/Ni HS (Fig. 1a) shows the combined peaks of FeOOH (JCPDS: 34-1266) and $Ni_2(CO_3)(OH)_2$ (JCPDS: 35-0501). The crystal structure simulations (Fig. S1a and b†) show the building units of the skeletal structure being MO_6 octahedra. The two peaks at 310 cm^{-1} and 380 cm^{-1} in the Raman spectrum of FeNi/Ni HS (Fig. 1b) correspond to the Fe–O vibration mode of octahedral Fe sites, while the peak at 720 cm^{-1} corresponds to the Fe–OH vibration.[33] The peak at 450 cm^{-1} is attributable to the vibration of Ni–O–Ni, while the one at 1058 cm^{-1} can be assigned to the vibration of CO_3^{2-}.[34] Significantly, the peak associated with the vibration of Ni–O–Fe of FeNi/Ni HS is found around 530 cm^{-1}.[35] These results confirmed that FeNi/Ni HS consists of FeOOH and $Ni_2(CO_3)(OH)_2$ with both being constructed with the octahedral MO_6 units and that the oxo-bridged octahedral units feature certain units of Ni–O–Fe due to the partial replacement of the Fe by Ni (Fig. 1c).

The morphology of FeNi/Ni HS was studied by SEM and TEM. The SEM image (Fig. 1d) showed a butterfly-like structure (inset 1d) featuring a "torso" of *ca.* 150 (length) × 20 nm

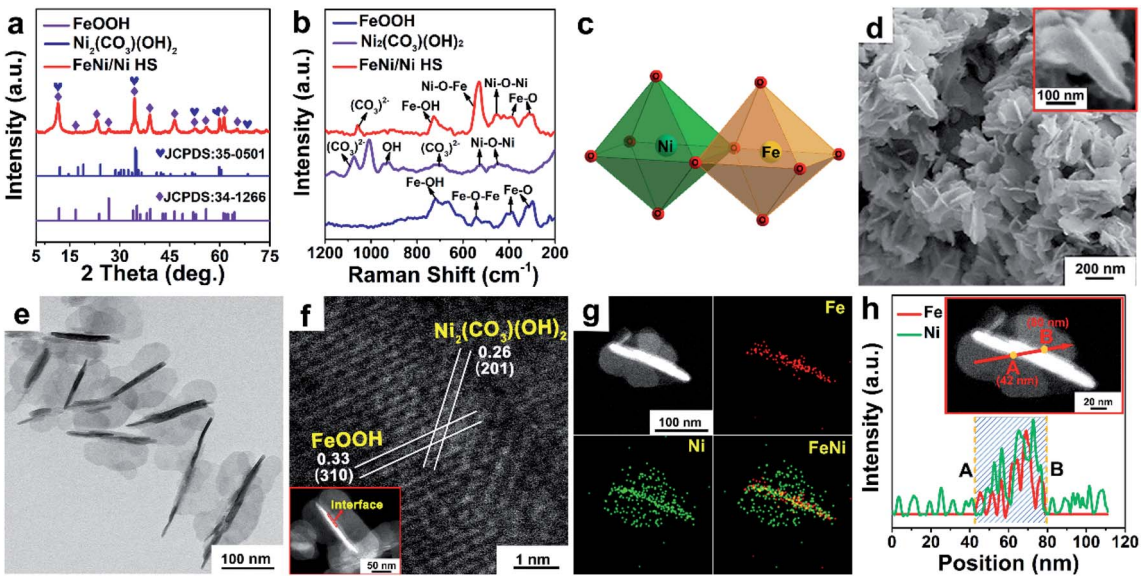

Fig. 1 Structural and morphological characterization of FeNi/Ni HS with respect to FeOOH and $Ni_2(CO_3)(OH)_2$. (a) X-ray powder diffraction (XRD) patterns. (b) Raman spectra. (c) The bimetallic arrangement mediated by the oxo bridge in FeNi/Ni HS. (d) Scanning electron microscopy (SEM) image (inset: a discrete butterfly-like unit of FeNi/Ni HS). (e) Transmission electron microscopy (TEM) image. (f) High-angle annular dark-field scanning transmission electron microscopy (HAADF-STEM) image showing the lattice fringes of FeNi/Ni HS (inset: the region where the fringes were captured). (g) HAADF-STEM image and the corresponding energy-dispersive X-ray spectroscopy (EDX) elemental mapping images of FeNi/Ni HS. (h) EDX line scan across FeNi/Ni HS (inset: the line scan position).

(width), flanked by two "wings" of *ca.* 50 nm (width). The butterfly-like structures with the length in the range between 100 and 150 nm and the width at *ca.* 100 nm are further shown in the TEM images (Fig. 1e and S2†). High-resolution lattice fringes of the interface are clearly shown in the HAADF-STEM image (Fig. 1f). The interplanar spacing of 0.33 nm within the "torso" can be indexed to the (310) plane of FeOOH with that of 0.26 nm in the "wings" to the (201) plane of $Ni_2(CO_3)(OH)_2$. The EDX elemental mapping (Fig. 1g and h) showed that the presence of Ni is concentrated in the "wings" while both Fe and Ni are present within the "torso", indicating a higher concentration of Ni than Fe in the heterostructure, which is also consistent with the results obtained by inductively coupled plasma (ICP) analysis (Table S1†). HAADF-STEM, EDX-mapping, and EELS were used to explore the location and electronic state of the "torso" Ni sites (Fig. S3†); they, as isolated atoms, are incorporated into the lattice of FeOOH to afford Ni-doped FeOOH. On the basis of the results by XRD and Raman spectroscopic analyses, it is reasonable to conclude that the "torso" is made primarily of Ni-doped FeOOH, while the "wings" are made essentially of pure $Ni_2(CO_3)(OH)_2$.

Synthesis mechanism

The present gelatin-induced formation of the heterostructure was made possible by the large number of metal-coordinating functional groups including –CO–NH_2, –COOH, and –NH_2 in gelatin (Fig. S4†). Preferential growth of a particular structure may be induced due to the differences in the coordination modes of these functional groups.[36,37] In this work, the gradual development of the butterfly-like heterostructure is clearly shown in the time-dependent evolution of FeNi/Ni HS as monitored by the EDX elemental mapping over a course of 36 hours. Specifically, four distinct stages, namely the formation of nanorods, nanorods with burrs, fragmental nanorods, and butterfly-like nanorods (Fig. 2 and S5†), are observed along the course of the heterostructure development. Specifically, 3 hours after the reaction with a mixture of $FeCl_3 \cdot 6H_2O$, $NiCl_2 \cdot 6H_2O$, urea, and gelatin, nanorods with co-existing Fe/Ni metal ions were observed (Fig. 2a and S5a†). Upon extending the reaction time to 6 hours, epitaxial growth on the nanorods occurred, producing nanorods with burrs that contained only Ni as indicated by EDX elemental mapping (Fig. 2b and S5b, c†). Further extending the reaction time to 18 hours resulted in the continuous growth of the burrs into plate-like fragments; only Ni was found in these fragments (Fig. 2c and S5d–f†). The butterfly-like heterostructure was achieved upon further extending the growth process up to 36 hours (Fig. 2d and S5g, h†). The change of the contents of Ni and Fe over this course is summarized in Table S2.† Besides, other reaction conditions including the amount of gelatin and urea, and the metal/organic stoichiometry have also been found to influence the morphology of the resulting heterostructures (Fig. S6†). Of particular note is the further epitaxial growth of the "wings" as the amount of Ni in the reaction mixture increased. This observation is consistent with the aforementioned concentration of only Ni in the wings when the reaction time was extended.

Electrocatalytic performance

A series of experiments were used to evaluate the catalytic performance of FeNi/Ni HS with references to FeOOH and $Ni_2(CO_3)(OH)_2$ (Fig. S7†) where appropriate. The linear sweep voltammetry curve (LSV) is shown in Fig. 3a. The onset overpotential of 220 mV for FeNi/Ni HS is significantly lower than those of FeOOH, $Ni_2(CO_3)(OH)_2$, a mixture of FeOOH and $Ni_2(CO_3)(OH)_2$ (FeOOH&$Ni_2(CO_3)(OH)_2$), Ni-doped FeOOH, commercial IrO_2, and GCE. Its overpotential of 268 mV to reach a current density of 10 mA cm^{-2} is also much lower than those of the comparison group. The corresponding catalytic performance of heterostructures with different Ni/Fe ratios has also been evaluated, and we found the heterostructure with a Ni/Fe ratio of 3/2 showing the best performance (Fig. S8†). This sample was then used for comparative studies discussed below.

The electrochemical active surface area (ECSA)-normalized current density (j_{ECSA}) is a parameter indicating the intrinsic activity of a catalyst and can be estimated from the electric double-layer capacitance (C_{dl}, Fig. S9†) obtained from a non-Faraday interval cyclic voltammetry curve (CV, Fig. S10†). As indicated by the ECSA-normalized current curves (Fig. 3b), FeNi/Ni HS operated with the lowest overpotential at 0.5 mA cm_{ECSA}^{-2}, indicating that the heterostructured catalyst is the most active one, followed by Ni-doped FeOOH, FeOOH&$Ni_2(CO_3)(OH)_2$, $Ni_2(CO_3)(OH)_2$, and FeOOH.[38,39] The mass activity (MA) and turnover frequency (TOF) of the catalysts were estimated (Table 1) with FeNi/Ni HS exhibiting the highest MA of 35.00 A g^{-1} and TOF of 0.0160 s^{-1}. Furthermore, electrochemical impedance plots (EIS, Fig. 3c) show a charge transfer resistance (R_{ct}) of 26 Ω for FeNi/Ni HS. This value, much smaller

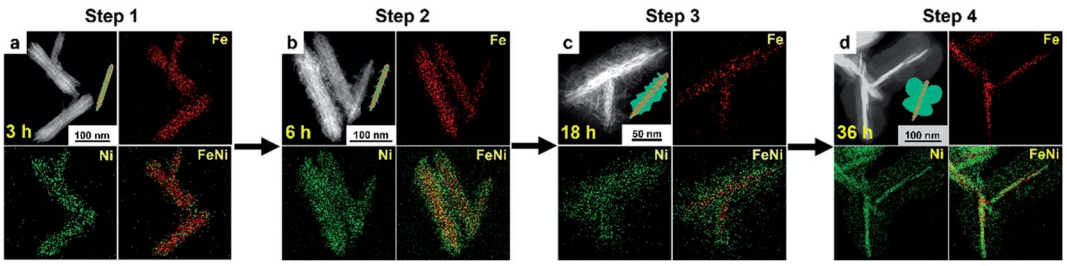

Fig. 2 Showing the growth of FeNi/Ni HS monitored by the EDX elemental mapping over a course of 36 hours. (a) Nanorods of 3 h stage. (b) Nanorods with burrs of 6 h stage. (c) Fragmental nanorods of 18 h stage. (d) Butterfly-like nanorods of 36 h stage.

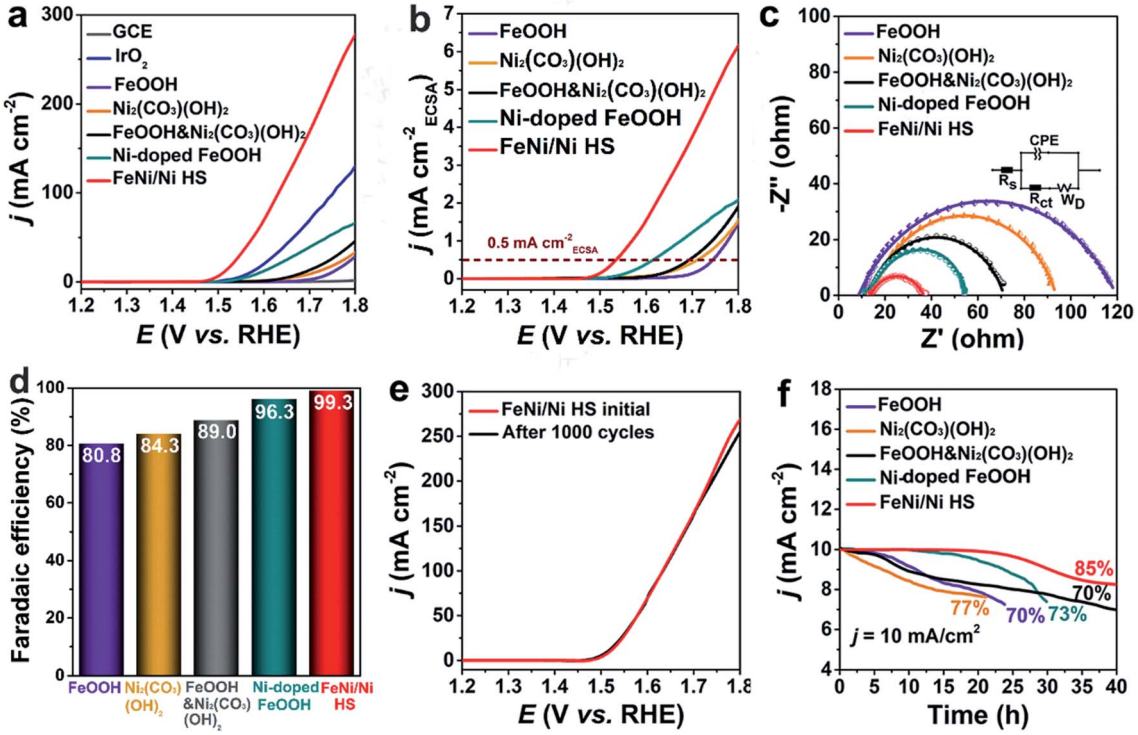

Fig. 3 Comparative electrochemical studies. (a) LSV curves. (b) ECSA-normalized current density curve. (c) Nyquist plots. (d) Faradaic efficiency of the catalysts in the comparison group. (e) LSV curves of FeNi/Ni HS were measured before and after 1000 cycles. (f) The chronopotentiometry curve of FeNi/Ni HS at 10 mA cm^{-2} during a 40 h period.

than those obtained for the catalysts in the comparison group (FeOOH 109 Ω, $Ni_2(CO_3)(OH)_2$ 82 Ω, FeOOH&$Ni_2(CO_3)(OH)_2$ 61 Ω, and Ni-doped FeOOH 45 Ω), indicates a much-enhanced charge-transfer characteristic of the heterostructured catalyst. The Nyquist plots, showing the feature of double-layer capacitance, were fitted by the equivalent circuit (inset Fig. 3c).

The faradaic efficiencies of the catalysts were also calculated (Fig. 3d and S11†) with FeNi/Ni HS producing the largest ring current of 39.7 μA (collection efficiency 0.2) among the comparison group and the highest faradaic efficiency of 99.3%.[40,41]

Long-term durability is necessary for practical applications. FeNi/Ni HS showed only a slight decrease of current density at high potential (Fig. 3e) after 1000 cycles. Moreover, chronopotentiometry measurement (Fig. 3f) shows that 85% of its original activity was maintained after 40 h of operation at 10 mA cm^{-2}. This stability performance is much better than that of the catalysts in the comparison group. TEM, XRD and XPS characterizations were used to further assess the stability of FeNi/Ni HS after long-term tests. The TEM image (Fig. S12a†) showed little morphological changes. In addition, the XRD patterns of the samples before and after the experiments (Fig. S12b†) are essentially the same. The valence states of the elements in the samples before and after the OER tests were evaluated by comparative XPS studies. While the binding energy of Fe 2p peaks remained essentially unchanged (Fig. S13a†), those of Ni $2p_{3/2}$ and Ni $2p_{1/2}$ (Fig. S13b†) shift to more positive values after the OER test, suggesting an increase of the higher-

Table 1 Comparison of electrocatalytic performances

Materials	Onset potential (V *vs.* RHE)	Overpotential[a] (mV)	MA (A g^{-1})	TOF (s^{-1})
FeNi/Ni HS	1.45	268	35.00	0.0160
FeOOH	1.65	514	0.36	0.0002
$Ni_2(CO_3)(OH)_2$	1.56	480	1.40	0.0006
FeOOH&$Ni_2(CO_3)(OH)_2$	1.55	450	2.24	0.0010
Ni-doped FeOOH	1.50	353	3.30	0.0014
IrO_2	1.53	340	—	—

[a] At a current density of 10 mA cm^{-2}.

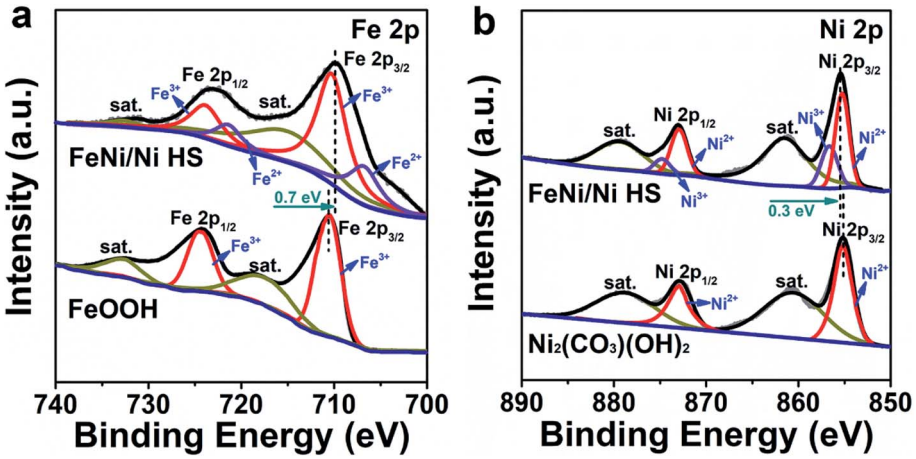

Fig. 4 XPS spectra of (a) Fe 2p and (b) Ni 2p electrons for FeNi/Ni HS with reference to FeOOH and $Ni_2(CO_3)(OH)_2$, respectively.

valance Ni^{3+} when compared with the sample before the test. This increase is corroborated by the decrease in the ratio of Ni^{2+}/Ni^{3+} from 1.87 to 1.53, indicative of the oxidation of Ni^{2+}.[42] In addition, we also compared FeNi/Ni HS with other transition metal-based catalysts (Table S3†); this heterostructured catalyst clearly possesses activity and stability that are superior to those in the literature.

Mechanistic analysis

As catalysis is primarily a surface-determined event, the most important factor affecting the activity of a catalyst is the electronic structure of the surface-bound atoms. To probe the electronic structures of these active sites, we conducted a series of comparative studies in order to differentiate between distinct regions of the heterostructure.

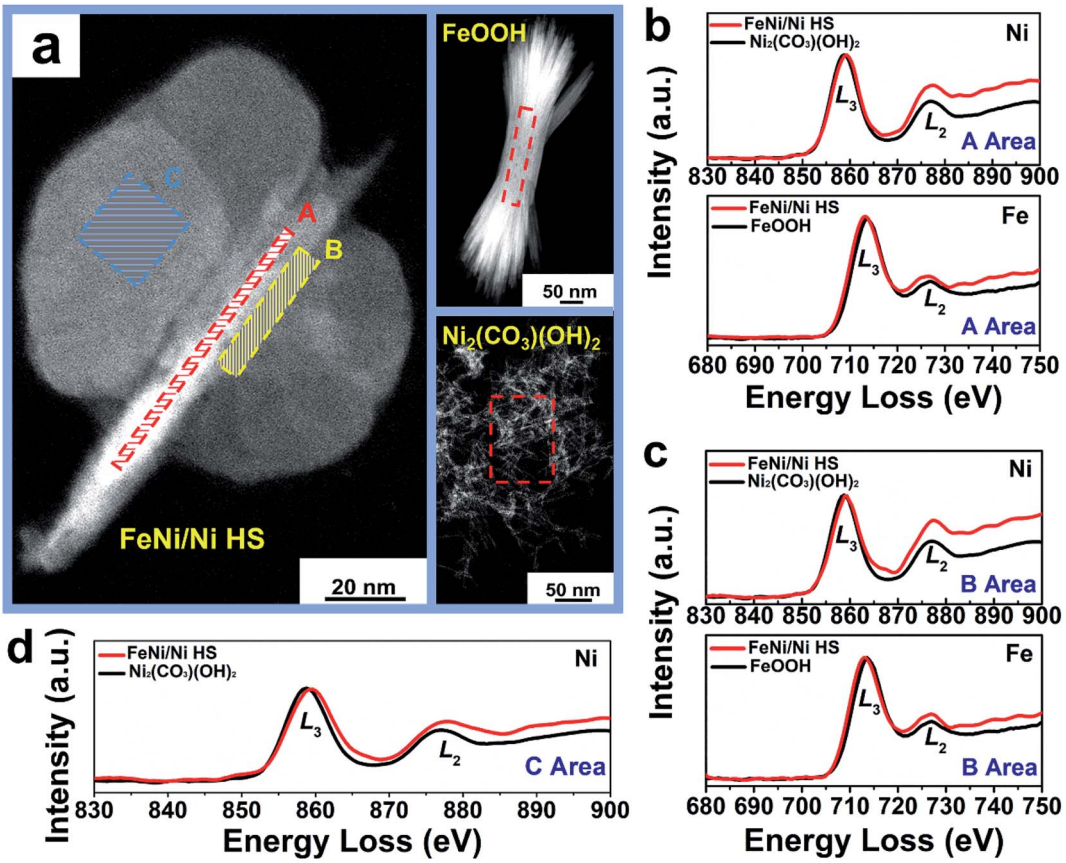

Fig. 5 EELS characterization of FeNi/Ni HS *versus* FeOOH and $Ni_2(CO_3)(OH)_2$. (a) HAADF image. (b) EELS spectra of Ni $L_{2,3}$ edges and Fe $L_{2,3}$ edges extracted in the "torso" (region A, red box in (a)). (c) EELS spectra of Ni $L_{2,3}$ edges and Fe $L_{2,3}$ edges extracted at the "torso–wing" interface (region B, yellow box in (a)). (d) EELS spectra of Ni $L_{2,3}$ edges extracted along with the "wing" (region C, the blue box in (a)).

Table 2 Calculated Fe L_3/L_2 and Ni L_3/L_2 ratios of catalysts

References	Fe L_3/L_2[a] (area ratio)	Ni L_3/L_2[b] (area ratio)
FeOOH	2.40	—
$Ni_2(CO_3)(OH)_2$	—	1.43
FeNi/Ni HS	**Fe L_3/L_2[a] (area ratio)**	**Ni L_3/L_2[b] (area ratio)**
A area (torso)	2.26 (5.8%↓)	1.18 (17.5%↓)
B area (torso–wing)	2.23 (7.1%↓)	1.23 (14.0%↓)
C area (wing)	—	1.29 (9.8%↓)

[a] A decrease of Fe L_3/L_2 area ratio indicates the increase of Fe^{2+}. [b] A decrease of Ni L_3/L_2 area ratio indicates the increase of Ni^{3+}.

To explore the electronic structures of Ni and Fe in FeNi/Ni HS, XPS analyses were undertaken. The Fe 2p spectrum (Fig. 4a) is fitted into two pairs of peaks, corresponding to Fe^{3+} (710.6 eV, 724.5 eV) and Fe^{2+} (707.0 eV and 723.0 eV),[24,42] respectively. Compared with the FeOOH reference, the binding energies of Fe 2p electrons in FeNi/Ni HS are lowered by 0.7 eV, indicating an increase of electron density due to the increase of Fe^{2+}. This assessment is corroborated by the increase of Ni^{3+} in FeNi/Ni HS as the binding energies of Ni 2p electrons in the heterostructure show a positive shift by 0.3 eV with respect to the reference $Ni_2(CO_3)(OH)_2$ (Fig. 4b).[43,44] Together, these oxidation-state changes may be attributable to the Ni^{2+}-to-Fe^{3+} electron transfer upon formation of the heterostructured catalyst.

Atomic electronic structure, in particular the valence state, is sensitively dependent on the chemical environment of the atoms of interest.[45] With respect to the references FeOOH and $Ni_2(CO_3)(OH)_2$, comparative electronic structure analyses by EELS of the "torso" (region A), the "torso–wing" interface (region B), and the "wing" (region C) of FeNi/Ni HS reveal the disparate electronic structures of the metal ions in these different regions of the heterostructure (Fig. 5a). Specifically, the area ratio of the Fe $L_{2,3}$ edges is 2.40, while that in region A ("torso") of FeNi/Ni HS is 2.26 (Fig. 5b and Table 2); the decrease by 5.8% indicates an increase of Fe^{2+} upon formation of the heterostructure.[46] An analogous analysis of the Ni L_3/L_2 edge area ratio in the same region revealed a decrease by 17.5% from 1.43 for $Ni_2(CO_3)(OH)_2$ to 1.18 for the heterostructure, which is indicative of an increase of Ni^{3+}.[47] In other words, both Fe^{2+} and Ni^{3+} increase in this region. The same conclusion can be reached qualitatively for the torso–wing interface (region B) on the basis of the EELS analyses (Fig. 5c and Table 2). These results unambiguously suggest the occurrence of electron transfer between Ni^{2+} and Fe^{3+} in the "torso" and at the "torso–wing" interface of the heterostructure and presumably by way of the Ni–O–Fe linkage: the π-symmetry d-orbitals (t_{2g}, $3d^8$) of Ni^{2+} are filled with electrons, causing an electronic repulsion between Ni^{2+} and the bridging O^{2-} ($2p^6$). In comparison, the t_{2g} ($3d^5$) orbitals of Fe^{3+} are half-filled. As such, it is reasonable to assume that electron transfer occurred initially *via* π-donation from the bridging O^{2-} to Fe^{3+}; this event is followed by a subsequent shift of electron density from Ni^{2+} to O^{2-}, leading to the net Ni^{2+}-to-Fe^{3+} electron transfer (Fig. S14†).[48]

In the wings (region C), the Ni L_3/L_2 edge area ratio is 1.29, decreasing from 1.43 of $Ni_2(CO_3)(OH)_2$ and suggesting an increase of Ni^{3+} (Fig. 5d and Table 2). This increase of Ni^{3+} can be attributed to the presence of Ni vacancies from intrinsic $Ni_2(CO_3)(OH)_2$ (Fig. S15a†) upon formation of the heterostructure as required by the charge balancing between Ni and O ions; there are simply not enough Ni^{2+} ions to balance the negative charge of O^{2-} from CO_3^{2-} and OH^- in $Ni_2(CO_3)(OH)_2$.

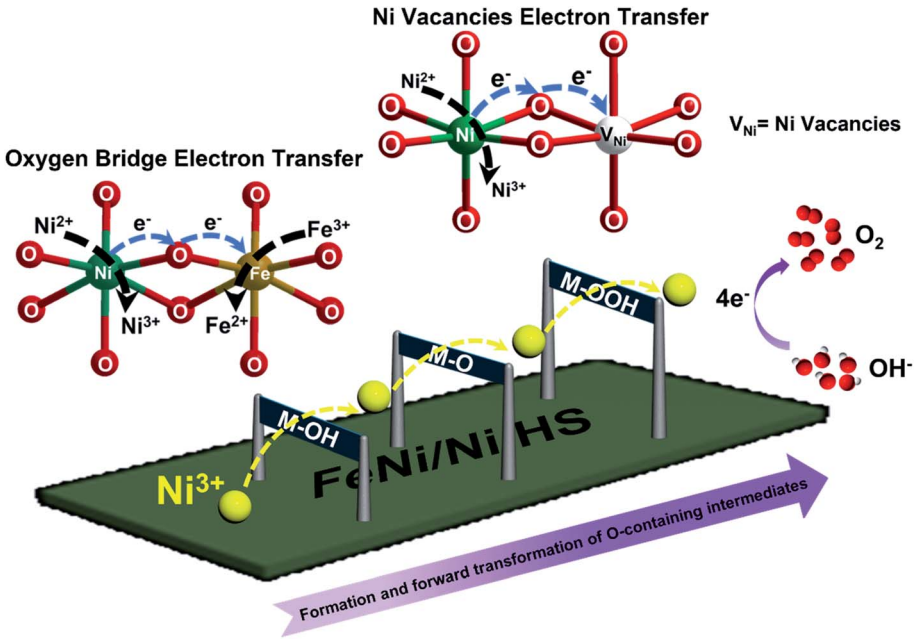

Fig. 6 Pictorial description of the electronic interplay between Ni, O, and Fe sites in FeNi/Ni HS involved in the mechanism possibly responsible for the present electrocatalytic OER under basic conditions.

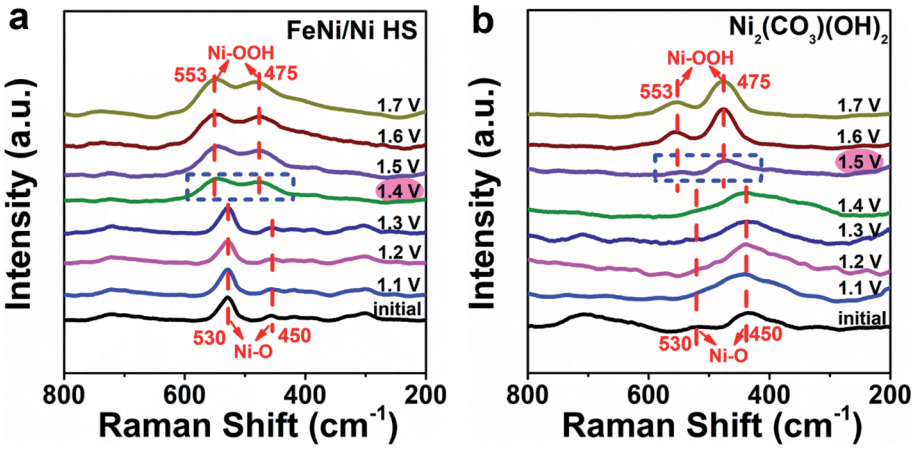

Fig. 7 Monitoring the formation of the Ni–OOH intermediate during the OER by *in situ* Raman spectroscopy; (a) FeNi/Ni HS was used as the catalyst *versus* (b) $Ni_2(CO_3)(OH)_2$ as the reference.

As such, an enhancement of the oxidation state from Ni^{2+} to $Ni^{(2+\delta)+}$ is anticipated (Fig. S15b†).[49]

With the above results, a mechanism possibly responsible for the observed catalytic OER by FeNi/Ni HS is schematically illustrated in Fig. 6. The increase of the higher-valence Ni^{3+} upon formation of the heterostructure within the "torso" and at the "torso–wing" interface is believed to be primarily responsible for the enhanced catalytic performance observed. With respect to other metal ions (Fe^{3+}/Fe^{2+}/Ni^{2+}) present, the more strongly Lewis acidic Ni^{3+} ions facilitate and strengthen the binding and thus activation of OH^- at the initial stage of the catalysis and forge ahead with the forward and successive transformation of the oxygen-containing intermediates (M–OH, M–O, M–OOH), leading eventually to the accelerated OER.

The specific enhancing effect of FeNi/Ni HS in promoting the formation and transformation of the oxygen-containing intermediates was investigated by *in situ* Raman spectroscopy (Fig. 7 and S16†). As shown in Fig. 7a, the peaks at 450 and 530 cm^{-1} up to 1.3 V are attributed to the Ni–O vibrations.[50] Starting from 1.4 V and up, two new peaks, characteristic of the vibrations of the Ni–OOH intermediate, appear at 553 and 475 cm^{-1} accompanied by the disappearance of the original Ni–O vibration peaks.[51,52] In contrast, with the use of $Ni_2(CO_3)(OH)_2$ as the reference catalyst, the Ni–OOH vibration peaks did not appear until 1.5 V (Fig. 7b). Notably, the Raman spectrum of FeOOH (Fig. S16†) does not show any noticeable changes during this process, suggesting that (1) $Fe^{2+/3+}$ ions are not directly involved in the formation of the oxygen-containing intermediates; and (2) the electronic structure changes brought about upon forming the heterostructure, primarily in the increase of Ni^{3+}, are responsible for the facilitated OER as evidenced by the facilitated formation of Ni–OOH – the key intermediate immediately preceding the release of O_2 in the OER process.

Extension of the preparation method to the construction of heterostructured FeCo/Co HS

The gelatin-induced genesis and growth of mixed-metal hydroxide heterostructures was validated further by the successful preparation of congenic FeCo/Co HS (Fig. S17†) using $CoCl_2 \cdot 6H_2O$ in place of $NiCl_2 \cdot 6H_2O$ under otherwise identical preparative conditions. Catalytic property investigation indicated that FeCo/Co HS also outperformed FeOOH, $Co(CO_3)_{0.5}(OH)$, a physical mixture of FeOOH and $Co(CO_3)_{0.5}(OH)$ (FeOOH&$Co(CO_3)_{0.5}(OH)$), Co-doped FeOOH, and IrO_2.

Conclusions

We report in this work a general gelatin-induced synthetic strategy for constructing bimetallic heterostructured hydroxides. A butterfly-like FeNi/Ni heterostructure featuring a "torso" flanked by two "wings" with two distinct "torso–wing" interfaces was obtained and showed superior electrocatalytic performance for the OER. XPS and EELS analyses indicated that both Ni^{3+} and Fe^{2+} increase in the "torso" and "torso–wing" regions, due supposedly to the Ni^{2+}-to-Fe^{3+} electron transfer by way of oxo bridges. The presence of Ni vacancies in the "wings" also causes the increase of Ni^{3+} ions when compared with pure $Ni_2(CO_3)(OH)_2$. The highly Lewis acidic Ni^{3+} ions facilitate and strengthen the association of OH^- at the initial stage of the catalysis, thus accelerating the formation and forward transformation of the oxygen-containing intermediates. Ni–OOH – the intermediate immediately preceding the release of O_2 was indeed observed by *in situ* Raman spectroscopy at a lower potential than when $Ni_2(CO_3)(OH)_2$ was used as the reference. The obtainment of an analogous high-performing heterostructured FeCo/Co catalyst suggests that the present gelatin-induced synthetic approach may be really applicable for the preparation of other electrocatalytically active mixed-metal hydroxides.

Data availability

The data supporting the findings of this study are available in the manuscript and the ESI.†

Author contributions

F. Y. L. performed the experimental work, data analysis, drafting, and revision of the manuscript. Y. Y. L. and L. L. helped with data collection and analyses, and manuscript revision. W. L. assisted in collecting the *in situ* Raman spectroscopic data and handling the data processing. Z. G. L. supervised the use of the *in situ* Raman spectrometer and offered valuable discussion of the results. X. Y. Z. conducted conceptualization and supervision of the project, data analyses, and writing and editing of the manuscript. Z. P. Z. conducted conceptualization, funding acquisition, project administration, and editing of the manuscript.

Conflicts of interest

The authors declare no competing financial interest.

Acknowledgements

We gratefully acknowledge the financial support by Shenzhen Nobel Prize Scientists Laboratory Project (Grant No. C17213101, Z. Z.), Guangdong Provincial Key Laboratory of Catalysis (No. 2020B121201002, Z. Z.), Guangdong Provincial Key Laboratory of Energy Materials for Electric Power (2018B030322001, Z. Z.), A Start-up Fund from SUSTech (Y01216127, Y01216227, Z. Z.), Post-doctorate Scientific Research Fund for staying in (coming to) Shenzhen (K21217502, X. Z.), and Basic Research Project of the Science and Technology Innovation Commission of Shenzhen (JCYJ20190809115413414, Z. L.). This work was also partially supported by the start-up fund from Southern University of Science and Technology. The authors also acknowledge the assistance of Southern University of Science and Technology Core Research Facilities (SUSTech CRF) and Key Laboratory of Energy Conversion and Storage Technologies (Southern University of Science and Technology).

Notes and references

1 J. Eom, M. Hyun, J. Lee and H. Lee, *Nat. Energy*, 2020, **5**, 976–984.
2 J. Wang, J. Wang, Z. Kong, K. Lv, C. Teng and Y. Zhu, *Adv. Mater.*, 2017, **29**, 1703044.
3 S. S. Wu, Y. G. Zhu, Y. F. Huo, Y. C. Luo, L. H. Zhang, Y. Wan, B. Nan, L. J. Cao, Z. Y. Wang, M. C. Li, M. Y. Yang, H. Cheng and Z. G. Lu, *Sci. China Mater.*, 2017, **60**, 654–663.
4 H. L. Van, L. Laffineur, R. Campe, P. Perreault, S. W. Verbruggen and S. Lenaerts, *Energy Environ. Sci.*, 2021, **14**, 815–843.
5 Q. Zhou, Z. Shen, C. Zhu, J. Li, Z. Ding, P. Wang, F. Pan, Z. Zhang, H. Ma, S. Wang and H. Zhang, *Adv. Mater.*, 2018, **30**, 1800140.
6 R. Chen, S. F. Hung, D. Zhou, J. Gao, C. Yang, H. Tao, H. B. Yang, L. Zhang, Q. Xiong, H. M. Chen and B. Liu, *Adv. Mater.*, 2019, **31**, 1903909.
7 R. Liu, Y. Wang, D. Liu, Y. Zou and S. Y. Wang, *Adv. Mater.*, 2017, **29**, 1701546.
8 Y. Wang, L. Yan, K. Dastafkan, C. Zhao, X. Zhao, Y. Xue, J. Huo, S. Li and Q. Zhai, *Adv. Mater.*, 2021, **33**, 2006351.
9 J. Kang, X. Qiu, Q. Hu, J. Zhong, X. Gao, R. Huang, C. Wan, L. M. Liu, X. Duan and L. Guo, *Nat. Catal.*, 2021, **4**, 1050–1058.
10 Z. P. Wu, X. F. Lu, S. Q. Zang and X. W. Lou, *Adv. Funct. Mater.*, 2020, **30**, 1910274.
11 A. C. Garcia, T. Touzalin, C. Nieuwland, N. Perini and M. T. M. Koper, *Angew. Chem., Int. Ed.*, 2019, **58**, 12999–13003.
12 O. Diaz-Morales, I. Ledezma-Yanez, M. T. M. Koper and F. CalleVallejo, *ACS Catal.*, 2015, **5**, 5380–5387.
13 C. Kuai, C. Xi, A. Hu, Y. Zhang, Z. Xu, D. Nordlund, C. J. Sun, C. A. Cadigan, R. M. Richards, L. Li, C. K. Dong, X. W. Du and F. Lin, *J. Am. Chem. Soc.*, 2021, **143**, 18519–18526.
14 J. Chen, F. Zheng, S. J. Zhang, A. Fisher, Y. Zhou, Z. Wang, Y. Li, B. B. Xu, J. T. Li and S. G. Sun, *ACS Catal.*, 2018, **8**, 11342–11351.
15 L. Trotochaud, S. L. Young, J. K. Ranney and S. W. Boettcher, *J. Mater. Chem. A*, 2014, **136**, 6744–6753.
16 X. Y. Xiong, Z. Cai, D. J. Zhou, G. X. Zhang, Q. Zhang, Y. Jia, X. X. Duan, Q. X. Xie, S. B. Lai, T. H. Xie, Y. P. Li, X. M. Sun and X. Duan, *Sci. China Mater.*, 2018, **61**, 939–947.
17 P. Acharya, R. H. Manso, A. S. Hoffman, S. I. Perez Bakovic, L. Kékedy-Nagy, S. R. Bare, J. Chen and L. F. Greenlee, *ACS Catal.*, 2022, **12**, 1992–2008.
18 Z. An, H. Ma, H. Han, Z. Huang, Y. Jiang, W. Wang, Y. Zhu, H. Song, X. Shu, X. Xiang and J. He, *ACS Catal.*, 2020, **10**, 12437–12453.
19 W. Chen, B. Wu, Y. Wang, W. Zhou, Y. Li, T. Liu, C. Xie, L. Xu, S. Du, M. Song, D. Wang, Y. Liu, Y. Li, J. Liu, Y. Zou, R. Chen, C. Chen, J. Zheng, Y. Li, J. Chen and S. Y. Wang, *Energy Environ. Sci.*, 2021, **14**, 6428–6440.
20 J. X. Feng, S. H. Ye, H. Xu, Y. X. Tong and G. R. Li, *Adv. Mater.*, 2016, **28**, 4698–4703.
21 Z. W. Gao, J. Y. Liu, X. M. Chen, X. L. Zheng, J. Mao, H. Liu, T. Ma, L. Li, W. C. Wang and X. W. Du, *Adv. Mater.*, 2019, **31**, 1804769.
22 Q. Zhang, W. Xiao, W. H. Guo, Y. X. Yang, J. L. Lei, H. Q. Luo and N. B. Li, *Adv. Funct. Mater.*, 2021, **31**, 2102117.
23 J. H. Li, L. L. Wang, H. J. He, Y. Q. Chen, Z. R. Gao, N. Ma, B. Wang, L. L. Zheng, R. L. Li, Y. J. Wei, J. Q. Xu, Y. Xu, B. W. Cheng, Z. Yin and D. Ma, *Nano Res.*, 2022, **15**, 4986–4995.
24 K. Z. Li, B. C. Zhao, J. Bai, H. Y. Ma, Z. T. Fang, X. B. Zhu and Y. P. Sun, *Small*, 2020, **16**, 2001974.
25 T. Y. Liu and P. Diao, *Nano Res.*, 2020, **13**, 3299–3309.
26 M. Y. Zheng, K. L. Guo, W. J. Jiang, T. Tang, X. Y. Wang, P. P. Zhou, J. Du, Y. Q. Zhao, C. L. Xu and J. S. Hu, *Appl. Catal., B*, 2019, **244**, 1004–1012.
27 J. Lv, L. Wang, R. Li, K. Zhang, D. Zhao, Y. Li, X. Huang and G. Wang, *ACS Catal.*, 2021, **11**, 14338–14351.
28 B. Shao, Z. Liu, G. Zeng, Y. Liu, Q. Liang, Q. He, T. Wu, Y. Pan, J. Huang, Z. Peng, S. Luo, C. Liang, X. Liu, S. Tong and J. Liang, *Appl. Catal., B*, 2021, **286**, 119867.
29 X. Liu, C. Kan, X. Wang, X. Yang and L. Lu, *J. Am. Chem. Soc.*, 2006, **128**, 430–431.

30 H. Nassira, A. Sanchez-Ferrer, J. Adamcik, S. Handschin, H. Mahdavi, T. N. Qazvini and R. Mezzenga, *Adv. Mater.*, 2016, **28**, 6914–6920.
31 J. J. Calvin, A. S. Brewer and A. P. Alivisatos, *Nat. Synth.*, 2022, **1**, 127–137.
32 S. Dhakal, K. L. Kohlstedt, G. C. Schatz, C. A. Mirkin and M. O. Cruz, *ACS Nano*, 2013, **7**, 10948–10959.
33 J. Hu, S. Li, J. Chu, S. Niu, J. Wang, Y. Du, Z. Li, X. Han and P. Xu, *ACS Catal.*, 2019, **9**, 10705–10711.
34 L. Peng, N. Yang, Y. Yang, Q. Wang, X. Xie, D. Sun-Waterhouse, L. Shang, T. Zhang and G. I. N. Waterhouse, *Angew. Chem., Int. Ed.*, 2021, **60**, 24612–24619.
35 J. T. Kloprogge, L. Hickey and R. L. Frost, *J. Raman Spectrosc.*, 2004, **35**, 967–974.
36 X. Zang, W. S. Chen, X. L. Zou, J. N. Hohman, L. J. Yang, B. X. Li, M. S. Wei, C. H. Zhu, J. M. Liang, M. Sanhadasa, J. J. Gu and L. W. Lin, *Adv. Mater.*, 2018, **30**, 1805188.
37 M. Helminger, B. H. Wu, T. Kollmann, D. Benke, D. Schwahn, V. Pipich, D. Faivre, D. Zahn and H. Cölfen, *Adv. Funct. Mater.*, 2014, **24**, 3187–3196.
38 X. H. Sun, Q. Shao, Y. C. Pi, J. Guo and X. Q. Huang, *J. Mater. Chem. A*, 2017, **5**, 7769.
39 D. Voiry, M. Chhowalla, Y. Gogotsi, N. A. Kotov, Y. Li, R. M. Penner, R. E. Schaak and P. S. Weiss, *ACS Nano*, 2018, **12**, 9635–9638.
40 H. L. Fei, J. C. Dong, Y. X. Feng, C. S. Allen, C. Z. Wan, B. Volosskiy, M. F. Li, Z. P. Zhao, Y. L. Wang, H. T. Sun, P. F. An, W. X. Chen, Z. Y. Guo, C. Lee, D. L. Chen, I. Shakir, M. J. Liu, T. D. Hu, Y. D. Li, A. I. Kirkland, X. F. Duan and Y. Huang, *Nat. Catal.*, 2018, **1**, 63.
41 T. Y. Ma, S. Dai, M. Jaroniec and S. Z. Qiao, *J. Am. Chem. Soc.*, 2014, **136**, 13925.
42 C. Ye, J. Liu, Q. Zhang, X. Jin, Y. Zhao, Z. Pan, G. Chen, Y. Qiu, D. Ye, L. Gu, G. I. N. Waterhouse, L. Guo and S. Yang, *J. Am. Chem. Soc.*, 2021, **143**, 14169–14177.
43 C. Cao, D. D. Ma, Q. Xu, X. T. Wu and Q. L. Zhu, *Adv. Funct. Mater.*, 2019, **29**, 1807418.
44 H. Li, S. Chen, Y. Zhang, Q. Zhang, X. Jia, Q. Zhang, L. Gu, X. Sun, L. Song and X. Wang, *Nat. Commun.*, 2018, **9**, 2452.
45 Y. Tian, X. Liu, L. Xu, D. Yuan, Y. Dou, J. Qiu, H. Li, J. Ma, Y. Wang, D. Su and S. Zhang, *Adv. Funct. Mater.*, 2021, **31**, 2101239.
46 C. Wang, D. R. Baer, J. E. Amonette, M. H. Engelhard, J. Antony and Y. Qiang, *J. Am. Chem. Soc.*, 2009, **131**, 8824–8832.
47 X. Ren, C. Wei, Y. Sun, X. Liu, F. Meng, X. Meng, S. Sun, S. Xi, Y. Du, Z. Bi, G. Shang, A. C. Fisher, L. Gu and Z. J. Xu, *Adv. Mater.*, 2020, **32**, 2001292.
48 J. Jiang, F. F. Sun, S. Zhou, W. Hu, H. Zhang, J. C. Dong, Z. Jiang, J. J. Zhao, J. F. Li, W. S. Yan and M. Wang, *Nat. Commun.*, 2018, **9**, 2885.
49 Y. J. Wu, J. Yang, T. X. Tu, W. Q. Li, P. F. Zhang, Y. Zhou, J. F. Li, J. T. Li and S. G. Sun, *Angew. Chem., Int. Ed.*, 2021, **60**, 26829–26836.
50 L. Bai, S. Lee and X. Hu, *Angew. Chem., Int. Ed.*, 2021, **60**, 3095–3103.
51 J. Zhang, J. Liu, L. Xi, Y. Yu, N. Chen, S. Sun, W. Wang, K. M. Lange and B. Zhang, *J. Am. Chem. Soc.*, 2018, **140**, 3876–3879.
52 C. F. Li, L. J. Xie, J. W. Zhao, L. F. Gu, H. B. Tang, L. R. Zheng and G. R. Li, *Angew. Chem., Int. Ed.*, 2022, **61**, e202116934.